Carbon 253 (2026) 121425

Contents lists available at ScienceDirect

Carbon

journal homepage: www.elsevier.com/locate/carbon

Tuning surface phosphorus chemistry in metal-free carbon electrocatalysts for enhanced hydrogen evolution

Sergio García-Dalí [a,b,*], Javier Quílez-Bermejo [a], Denis Diatlov [c], Wouter Marchal [d], Elien Derveaux [d], Jimena Castro-Gutiérrez [a], María T. Izquierdo [e], Lluís Blancafort [c], Alain Celzard [a,f], Vanessa Fierro [a,**]

[a] Université de Lorraine, CNRS, IJL, F-88000, Épinal, France
[b] Departamento de Ciencia de Los Materiales e Ingeniería Metalúrgica, Universidad de Oviedo, 33004, Oviedo, Spain
[c] Institut de Química Computacional i Catàlisi i Departament de Química, Universitat de Girona C/M. A. Capmany 69, 17003, Girona, Spain
[d] UHasselt - Hasselt University, Institute for Materials Research (imo-imomec), Agoralaan building D, 3590, Diepenbeek, Belgium
[e] Instituto de Carboquímica (ICB-CSIC), Miguel Luesma Castán 4, E-50018, Zaragoza, Spain
[f] Institut Universitaire de France (IUF), 75231, Paris, France

ARTICLE INFO

Keywords:
Phytic acid
Phosphorus doping
Carbon
Metal-free catalyst
Pluronic® F-127

ABSTRACT

The precise modulation of phosphorus species and physicochemical properties in metal-free carbon materials holds significant potential for enhancing their electrocatalytic performance in the hydrogen evolution reaction (HER). In this study, we precisely tune the phosphorus species during the pyrolysis of phytic acid (PA). Pluronic® F127 acts as a protective agent, preventing the close proximity of phosphorus groups in PA molecules during pyrolysis. This interaction inhibits the formation of polyphosphoric groups during carbonization and leads instead to isolated P functionalities embedded in carbon basal planes. Comprehensive characterization, including cross-polarization magic angle spinning solid-state ^{31}P NMR, XPS, and DFT simulations identified the phosphorus species and elucidated their structural and electronic properties. The precise tuning of phosphorous functional groups enabled by Pluronic® F127 in metal-free carbon materials boosting the phosphorous based state-of-the-art HER catalytic performance. These findings underscore the underexplored potential of surfactants beyond morphological templating, offering a powerful strategy for tailoring surface chemistry and advancing the design of next-generation metal-free electrocatalysts.

1. Introduction

The widespread adoption of hydrogen as an energy carrier depends on the ability to produce it efficiently through processes such as water electrolysis, where the hydrogen evolution reaction (HER) plays a central role [1]. HER is the key to unlocking the potential of hydrogen as a clean energy source. However, this reaction is intrinsically sluggish and necessitates the use of expensive electrocatalysts to speed up the rate of H_2 production [2,3]. Currently, Pt nanoparticles anchored on carbon substrates represent the commercial electrocatalysts of choice for driving the HER [4,5]. Nevertheless, it is widely recognized that Pt-based electrocatalysts face global implementation challenges due to their limited availability, exorbitant price and susceptibility to degradation [6,7]. This is why the development of efficient and cost-effective catalysts for the HER has become a focal point of research in the broader field of electrocatalysis [8,9].

In recent years, the exploration of carbon-based materials as catalysts for the HER has gained significant attention [10–14], since they offer several advantages, including excellent electrical conductivity, chemical stability and the ability to be prepared from abundant precursor materials. In this context, the integration of nitrogen (N) as a heteroatom in carbon-based materials has emerged as a promising strategy [15,16]. The modulation of carbon's electronic structure and surface chemistry through N doping has been deeply studied in recent years. Consequently, the catalytic role of each type of N (graphitic, pyridinic, pyrrolic, …) in the carbon structure for different reactions is widely studied [17–20].

Despite remarkable progress in the investigation of heteroatom-

* Corresponding author. Université de Lorraine, CNRS, IJL, F-88000, Épinal, France.
** Corresponding author.
E-mail addresses: sergio.dali@icmse.csic.es (S. García-Dalí), vanessa.fierro@univ-lorraine.fr (V. Fierro).

https://doi.org/10.1016/j.carbon.2026.121425
Received 25 November 2025; Received in revised form 26 February 2026; Accepted 4 March 2026
Available online 6 March 2026

doped carbon materials for electrocatalytic applications, the role of phosphorus (P) remains relatively underexplored and is limited to the presence of P–C or P–O species [21,22]. The potential of phosphorus as a heteroatom in carbonaceous materials for HER is still far from being considered competitive [23,24]. This lack of comprehensive understanding highlights the need for further research to unravel the intricate interactions between phosphorus dopants and carbon matrices, and their influence on electrocatalytic performance for HER. On the other hand, Pluronic® F127 is a non-ionic surfactant widely used in materials synthesis, particularly in the preparation of mesoporous carbons by heat treatment of organic precursors [25]. This surfactant forms micelles in aqueous solutions and serves as a structure-directing agent, controlling the porous architecture of carbon-based materials. However, its use beyond the control of textural properties has never been explored.

Encouraged by the aforementioned motivations, various proportions of Pluronic® F-127 were employed during the carbonization of phytic acid (PA), with the aim of tailoring the chemical state of phosphorus and the physicochemical properties of the resulting carbon material. Extensive characterization was carried out, proving that P species in the resulting material can be modulated by varying the initial proportion of Pluronic® F-127. This systematic approach yielded promising results, manifested in improved electrocatalytic performance with an outstanding E_{HER} of −0.19 V vs RHE. Furthermore, DFT calculations provided insight into how different P species can modify the electronic and chemical properties of a carbon layer, and how this affects the electrocatalytic behavior of the resulting material.

2. Materials and methods

Phytic acid (PA) solution (50 wt% in water), Pluronic® F-127 and Nafion® (5 wt% in water) were supplied by Sigma Aldrich. Isopropanol (99.9 %) and potassium hydroxide (KOH, 85 %) were provided by VWR. All reactants were used as received.

PA-PX synthesis: The synthesis of PA-PX samples is founded on the optimal phosphorous doped carbon from PA preparation method as established in previous research [26]. Briefly, 4 g of PA solution (2 g PA + 2 g H_2O) is meticulously blended with varying quantities of Pluronic® F-127 (ranging from 1 to 7 g) at a stirring rate of 500 rpm. This mixing takes place in a 50 mL agate bowl containing 10 agate balls (1 cm in diameter) using a planetary ball mill (PM100, Retsch). Next, the resultant samples (PA-PX_mix) are subjected to a heat treatment process in a tubular furnace set at 900 °C for a duration of 1 h, employing a heating rate of 5 °C min^{-1} under a continuous flow of nitrogen (N_2) gas at a rate of 150 mL min^{-1}. Notably, prior to the heat treatment, the furnace undergoes a purge step at room temperature for 1 h, maintaining the same N_2 gas flow rate. Sample PA-P0, which consist exclusively in PA, was not subjected to ball-milling, but taken directly to heat treatment.

Physicochemical characterization: PA-PX samples were characterized by elemental analysis (EA), oxygen bomb digestion, N_2 adsorption-desorption, X-ray diffraction (XRD), transmission electron microscopy (TEM), X-ray photoelectron spectroscopy (XPS), solid-state nuclear magnetic resonance (NMR), thermogravimetric (TG) analysis and Raman spectroscopy.

The quantification of oxygen content (expressed as weight percentages, wt.%) was carried out by a direct analytical process using an Elementar Vario EL cube analyzer. This method involved subjecting approximately 2 mg of each sample to combustion at a high temperature of 1700 °C in an oxygen-containing helium atmosphere. The gases formed were then directed to a chromatographic column and were analyzed using a thermal conductivity detector, with the exception of sulfur-containing gases, which were quantified using an infrared detector. The absolute P content in the sample was investigated via a Parr® oxygen bomb digestion, followed by ion chromatography. The samples (approx. 0.25 g portions) were digested in duplicate using an oxygen-flushed reactor, after which the decomposition gases were trapped in 100 mL carbonate buffer. The samples were then analyzed on a Thermo ICS-6000 ion chromatography setup using an AS11 anion separation column.

N_2 adsorption-desorption isotherms were acquired at a cryogenic temperature of −196 °C using a fully automated ASAP2020 manometric adsorption apparatus manufactured by Micromeritics. To ensure the reliability of the adsorption experiments, the samples underwent a meticulous outgassing process under high vacuum conditions, typically ranging between 2 and 4 × 10^{-6} Pa (Pa). This outgassing procedure, performed at 90 °C, lasted a minimum of 24 h in the dedicated degassing port. Additionally, a further degassing step in the analysis port was conducted, lasting at least 6 h, prior to the introduction of successive N_2 doses. These doses were initially administered with the samples maintained under high-vacuum conditions. After N_2 adsorption-desorption, warm and cold volumes were measured to avoid helium trapping in the narrowest pores. H_2 adsorption-desorption isotherms at −196 °C were also obtained using the same procedure. Determination of the BET area (A_{BET}) of the materials was carried out in accordance with guidelines established by the International Union of Pure and Applied Chemistry (IUPAC) [27]. This calculation was performed using MicroActive® software developed by Micromeritics. Pore size distributions (PSDs) evaluation was based on Micromeritics' SAIEUS® software, applying the 2D non-local density functional theory for heterogeneous surfaces (2D-NLDFT-HS) to analyze N_2 and H_2 isotherms for all materials. Consequently, the total surface area (S_{NLDFT}) was calculated from the PSD data obtained for each respective material.

The structural characteristics of all carbon materials were assessed using a Bruker D8 Advance A25 X-ray diffractometer for polycrystalline powders. This instrument is equipped with a Cu anode X-ray source, operating at 40 kV and 40 mA, combined with a scintillation detector and a graphite monochromator for precise X-ray analysis. Silver behenate served as a reference material in the X-ray diffraction measurements.

For TEM imaging, a JEM – ARM 200 F Cold Field Emission Gun (FEG) TEM/STEM instrument equipped with probe and image spherical aberration correctors was employed. Sample preparation involved dispersion of the powdered material in ethanol using low-power sonication. A small quantity of the resulting suspension was then deposited on a carbon-coated copper TEM grid (200 mesh) and air-dried.

XPS spectra were acquired employing an OMICRON ESCAPlus spectrometer, which featured a non-monochromatized Mg Kα X-ray source. To enhance the accuracy of the spectral data, background subtraction using a Shirley-type model, peak fitting and subsequent quantification were carried out with CASA software.

Solid-state ^{31}P MAS and ^{31}P CPMAS (cross polarization magic angle spinning) NMR spectra were acquired at ambient temperature on an Agilent VNMRS DirectDrive 400 MHz spectrometer (9.4 T wide bore magnet) equipped with a T3HX 3.2 mm probe. MAS was performed at 15 kHz using 3.2 mm zirconia rotors. The signal of KH_2PO_4 was used to calibrate the phosphorus chemical shift scale (3.9 ppm). Acquisition parameters used were: a spectral width of 60 kHz, a 90° pulse length of 3.9 μs, an acquisition time of 12 ms, a recycle delay time of 10 s (MAS) or 3 s (CPMAS) and 1500 (MAS) or 5000 (CPMAS) accumulations. High power proton dipolar decoupling during the acquisition time was set to 80 kHz. For the 31P CPMAS measurements, the PA-P7 sample was used to determine the Hartmann-Hahn ($\omega_{1H} = \gamma_H B_{1H} = \gamma_C B_{1P} = \omega_{1P}$) and a contact time of 0.5 ms was used. Solid-state ^{13}C MAS NMR spectra were acquired at ambient temperature on a Bruker 400 MHz spectrometer (9.4 T) equipped with a 4 mm probe. MAS was performed at 15 kHz using 4 mm zirconia rotors. The aromatic signal of hexamethylbenzene was used to calibrate the carbon chemical shift scale (132.1 ppm). Acquisition parameters used were: a spectral width of 50 kHz, a 90° pulse length of 4.0 μs, an acquisition time of 15 ms, a recycle delay time of 20 s and 500 accumulations. High power proton dipolar decoupling during the acquisition time was set to 80 kHz.

To monitor the mass loss and decomposition processes occurring during carbonization, the PA-PX_mix samples, after the

mechanochemical step, were subjected to TG analysis. In this analytical procedure, the sample was gradually heated to 1000 °C at a controlled heating rate of 10 °C min^{-1}, while maintaining a continuous flow of argon gas (Ar) at a rate of 50 mL min^{-1}.

Raman spectra were collected using a Horiba Scientific XploRa Raman spectrometer equipped with a 50 × long-range objective and a red laser of wavelength 638 nm. The laser light was circularly polarized and filtered to 1% of its nominal power before being dispersed through a holographic grating with 1200 lines per millimeter. Each spectrum analyzed in this study represents the average of seven spectra acquired from seven distinct areas of the samples. Each of these seven spectra was obtained by accumulating two successive spectra over a 180-s interval, covering a Raman shift range between 800 and 2200 cm^{-1}. The final spectra underwent fitting procedures based on the methodology described by Mallet-Ladeira et al. [28] using a double Lorentzian model for the D band and a mixed Gaussian−Lorentzian asymmetric profile for the G band.

Electrochemical measurements: Electrochemical characterization of the PA-PX carbons was carried out in a conventional three-electrode cell configuration, incorporating a rotating ring-disk electrode (RRDE) connected to a Metrohm PGSTAT302 N bi-potentiostat. The working electrode was composed of a glassy carbon disk with an area of 0.196 cm^2, with a platinum ring serving as a second working electrode. A reversible hydrogen electrode (RHE) was employed as reference electrode, while an 8 mm diameter glassy carbon rod was utilized as counter electrode. All electrochemical measurements were conducted in an acidic electrolyte consisting of 0.5 M H_2SO_4 at room temperature. To prepare the working electrodes, a solution of isopropanol/water (20/80, v/v) with the addition of 0.2 wt% Nafion® was previously produced. Then, materials were suspended on it at a concentration of 4 mg mL^{-1}. Next, four 8.42 μL aliquots of the resulting ink were drop-cast onto the glassy carbon disk, yielding a carbon loading of 0.68 mg cm^{-2}. To optimize the wettability of the prepared electrodes, all materials were immersed in the working solution under vacuum for a brief period, in accordance with well-established electrode preparation methodology [29]. After this step, each electrode was introduced into the working solution with continuous nitrogen bubbling. Before starting the electrocatalytic study, cyclic voltammetry (CV) scans were conducted in the voltage range from 1.00 to 0.00 V versus RHE, employing a scan rate of 50 mV s^{-1} for a total of 20 cycles. This procedure stabilized the electrode. Next, linear sweep voltammetry (LSV) measurements were performed at 1600 rpm with a scan rate of 5 mV s^{-1}, spanning a range from 0.20 V to −0.80 V vs RHE. The recorded currents were consistently normalized based on the geometric area of the disk (0.196 cm^{-2}). The potential required to achieve a current density of −10 mA cm^{-2}, hereafter referred to as E_{HER}, was used as a benchmark to compare the catalytic activity of the materials examined. The stability of the electrocatalysts was evaluated by subjecting the electrodes to 1000 consecutive LSV cycles. The durability was quantified by monitoring the potential variation required to reach a current density of −10 mA cm^{-2} in each cycle. For comparison purposes, a commercial platinum-based electrocatalyst (Pt/C, from Sigma-Aldrich) was also evaluated under identical conditions in the electrocatalytic experiments.

Theoretical simulations: All calculations were performed using the Vienna Ab initio Simulation Package (VASP) version 5.2 with periodic boundary conditions (PBC). The Perdew-Burke-Ernzerhof (PBE) exchange-correlation functional within the generalized gradient approximation (GGA) was employed with projector augmented-wave (PAW) pseudopotentials [30]. A similar approach was used by one of us to model phosphorus-doped catalysts obtained from phytic acid pyrolysis [31]. Each modeled system was constructed from pristine graphite, incorporating a single carbon monolayer composed of 50 carbon atoms with a 14 Å vacuum. Graphene edge was simulated with hydrogen termination along the x-axis. Structural relaxation and total energy calculations used a plane-wave basis set with a 400 eV energy cutoff and a 2 × 2 × 1 Monkhorst-Pack k-point grid. A Gaussian smearing with a 0.1 eV width was applied and electronic optimizations were converged to within 1 × 10^{-6} eV. Nudged Elastic Band (NEB) calculations were carried out to find out the energy barrier. Gibbs free energies were obtained by additional frequency calculations according to the following equations:

$$\Delta G_H^* = \Delta E_H + \Delta E_{ZPE} - T\Delta S_H \quad (1)$$

Where:

ΔE_H (ΔDFT energy) is calculated using the following equation:

$$\Delta E_H = E_{surf\text{-}H} - (E_{surf} + E_{1/2H2}) \quad (2)$$

ΔE_{ZPE} (Zero Point Energy correction) is computed using vibrational frequency calculation of the H atoms in the system for reactants, transition states and products. E_{ZPE} is assumed constant for the surface throughout the reaction and is not considered in the vibrational frequency calculations.

$T\Delta S_H$ (vibrational entropy) is approximated as $T\Delta S_H \cong -1/2S_0$ (for the Volmer reaction), where S_0 is the entropy of H_2 in the gas phase at standard conditions. $T\Delta S_H$ is estimated to be 0.2 eV [32].

To determine the Gibbs energy correction along the NEB calculations, the calculated shift from reactants to products was interpolated, applying a scaling factor at each step using the H–H bond distance as the reaction coordinate.

For the Heyrovsky mechanism, proton adsorption was simulated using a water cluster consisting of three H_2O molecules, one of which takes the form of a hydronium ion (H_3O^+) adsorbed above the surface. This model captures the main solvation effects on H_3O^+, with two water molecules hydrogen bonded to two of the hydrogen atoms of the ion, leaving the third hydrogen atom free to react with the chemisorbed hydrogen atom. The negative charge is delocalized at the surface, resulting in an electroneutral system.

We have also considered the use of a dispersion correction. As a test, the free energy barrier along the Heyrovsky path was recalculated for the PO_2 system at the PBE + D3 level, doing single-point calculations at the PBE optimized geometries. Inclusion of the D3 dispersion correction reduces the barrier from 0.18 to 0.16 eV. The small effect is probably related with the fact that the interactions between the H_3O^+ ion and the negatively charged H_{ads} are dominated by electrostatic interactions, and dispersion effects are comparatively small. In turn, the Volmer step is simulated by calculations that involve the bare surface and the chemisorbed hydrogen atom (H_{ads}) with a covalent C–H bond, and dispersion effects will be also small. On the basis of these considerations, and given that the Volmer and Heyrovsky paths are the main paths of our proposed mechanism, we have decided not to apply the dispersion correction.

For NMR chemical shift calculations, the plane-wave energy cutoff was increased to 600 eV, and the accuracy of electronic optimization was tightened to 1 × 10^{-8} eV. Spin-polarization was included in the open-shell systems. To validate the periodic model results further, we employed corresponding molecular systems optimized using ORCA 5.3 at the PBE level of theory with the def2-SVP basis set for benchmarking purposes. The reference molecule for all systems in the NMR study was H_3PO_4.

3. Results and discussion

3.1. Synthesis and morphological characterization

Mixtures containing different amounts of PA and Pluronic® F-127 were prepared by a mechanochemical step. As detailed in the Experimental section, PA-PX materials (where X represents the mass content of Pluronic® F-127) were synthesized from these mixtures. Representative photographs of the mixtures obtained after the mechanochemical process are shown in Fig. S1. As can be observed, PA-P1 appears as a liquid-like phase due to the high proportion of PA and water. With increasing Pluronic® F-127 content, the mixtures evolve into pastes that are

progressively richer in Pluronic® F-127 and exhibit a less fluid and more consistent texture, reflecting the decreasing relative amount of aqueous PA.

This was followed by heat treatment at 900 °C (Fig. 1a), the temperature at which the highest proportion of C–P species has been found previously [26].

TEM images, shown in Fig. S2, reveal crucial insights into the structural characteristics of phosphorus-doped carbons. Interestingly, despite diverse formulations utilizing different concentrations of Pluronic® F-127, the morphological features clearly remain unchanged.

Nitrogen adsorption-desorption isotherms at 77K are shown in Fig. 1b. In general, as the amount of Pluronic® F-127 increased, nitrogen uptake at low relative pressure decreased, indicating a loss of microporosity (pores whose width, w, is less than 2 nm). This behavior is clearly observed on the PSDs of Fig. S3 and Table S1 and is the main reason for the decrease in apparent A_{BET} of the materials with increasing Pluronic® F-127 content, see Table S1. On the other hand, carbonization of pure PA (sample PA-P0) resulted in a material with a broad distribution of mesopores ($2 < w < 50$ nm). The formation of these pores can be attributed to the thermal decomposition of phosphate groups present in PA [26]. At low Pluronic® F-127 contents, interactions between adjacent PA molecules promote the growth of longer polyphosphate chains. During pyrolysis, the evolution of these larger chains generates more extensive microporosity and mesoporosity, increasing the surface area. Conversely, higher amounts of Pluronic® F-127 hinder intermolecular interactions of PA, leading to more isolated phosphate groups. Upon thermal treatment, the decomposition of these isolated groups produces smaller, less interconnected pores, resulting in lower overall surface area and porosity. The addition of Pluronic® F-127 significantly reduced the presence of mesopores, particularly those with $w > 6$ nm, most likely due to the water present in the PA solution. Under such conditions, Pluronic® F-127 indeed promotes the formation of micelles, leading to the formation of carbon structure around them and creating narrower mesopores. For high quantities of Pluronic® F-127 (PA-P4 to PA-P7), the textural properties of the obtained materials did not change significantly, as the surface area and the micro- and mesopore volume remained relatively constant, see again Table S1.

XRD patterns of the phosphorous doped carbon materials are presented in Fig. 1c. These patterns collectively reveal a distinctive and broad (002) diffraction band, conspicuously centered at $2\theta = 23°$. This is characteristic of highly disordered carbons, in which the parallel alignment of aromatic carbon sheets undergoes random twisting, introducing structural disorder. Notably, as the quantity of Pluronic® F-127 increases, a noticeable trend emerges: the (002) diffraction peak undergoes a discernible shift towards lower angles. This intriguing shift suggests the potential presence of graphite sheets with relatively greater interlayer spacing [33]. Simultaneously, a second distinct diffraction band becomes apparent, centered at $2\theta = 43°$. This band, referred to as (101), signifies the emergence of order in the planar direction of the carbon structure [34]. It strongly implies the existence of well-defined graphitic domains within the carbon matrix, further underscoring the structural evolution driven by varying the Pluronic® F-127 content [34].

The 1st-order Raman spectra of PA-P0, PA-P2 and PA-P6, as representative samples in Fig. 1d (with the remaining series presented in Fig. S4), reveal two primary bands typical of carbon materials. The D band, appearing around 1350 cm^{-1}, indicates defects within the carbon layers and heteroatoms, while the G band, at 1590 cm^{-1}, corresponds to the C–C elongation mode in the aromatic rings, indicative of sp^2 carbon vibrations. However, the I_D/I_G ratio (shown in Table S2), typically used

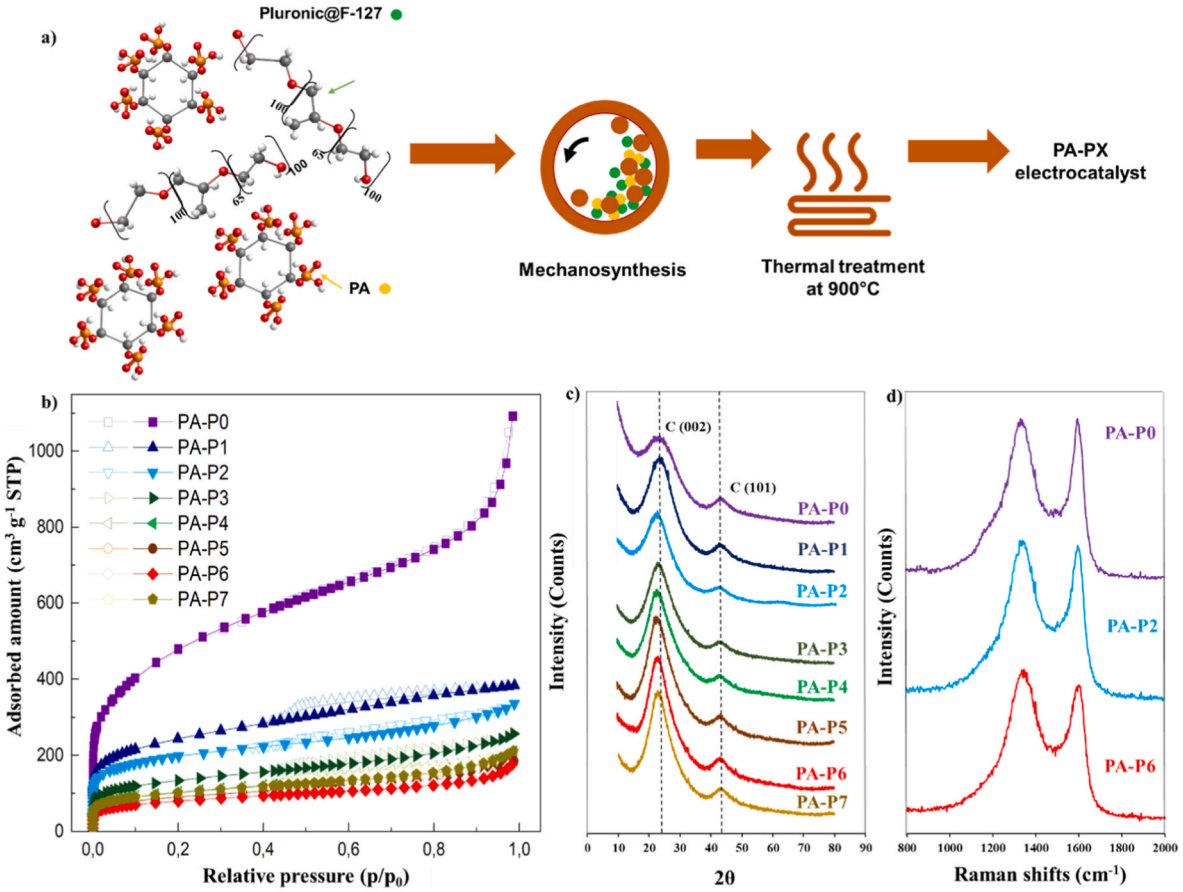

Fig. 1. a) Scheme of the PA-PX synthesis process from PA and Pluronic® F-127. b) N_2 adsorption (solid symbols) – desorption (empty symbols) isotherms, and c) XRD patterns of all PA-PX materials. d) Raman spectra of selected samples PA-P0, PA-P2 and PA-P6.

as an indicator of graphitization, is influenced differently in non-graphitizable carbon materials. In this study, characterized by oxygen-rich precursors and predominance of sp^3 carbons, a higher proportion of Pluronic® F-127 in the synthesis increases the I_D/I_G ratio and shifts the G band towards 1600 cm^{-1}, contrary to the behavior of 100% sp^2 carbons. This "carbonization" regime, distinct from "graphitization" [35], changes the relationship between the I_D/I_G ratio and the size of the coherent domains (L_a) from $1/L_a$ (graphitization regime) to L_a^2 (carbonization regime) [36]. The observed increase in I_D/I_G ratio with higher Pluronic® F-127 content suggests better ordering at the nano-scale, which is consistent with XRD results. Moreover, the shift to higher G-band values in samples with higher Pluronic® F-127 content corresponds to the 2nd stage of the ordering trajectory, as described by Ferrari and Robertson [37].

3.2. Structural characterization revealing the nature of phosphorus species

Table 1 reports the results of bulk and surface phosphorus content, determined by oxygen bomb combustion coupled with ion chromatography analysis (CIC) and XPS, respectively. Both contents provide crucial insights into the heteroatom composition of the resulting materials. The quantity of Pluronic® F-127 appears to be a determining factor in setting this heteroatom content. The discrepancies between bulk and surface chemistry (both in Table 1) suggest that the increased presence of Pluronic® F-127 promotes surface P enrichment rather than bulk incorporation. In samples featuring lower amounts of Pluronic® F-127 (from PA-P0 to PA-P2), the phosphorus content on the surface remains unchanged at around 4-5 at.%. However, the surface phosphorus content increases when using higher amounts of Pluronic® F-127, from PA-P3 to PA-P7, without exceeding a maximum of around 7.5 at.%.

Fig. 2apresents P 2p XPS spectra for the entire PA-PX series, revealing a rise in the proportion of C–P species (133.0 eV) versus C–*O*–P (134.2 eV) species [38] with increasing Pluronic content, with a peak in sample PA-P6. The excess of Pluronic@F-127 in PA-P7 probably provides an excess of oxygenated groups that could preserve phosphorus under its oxidized form (C–*O*–P species), as observed by the reduction in the P–C/P_T ratio. Additionally, C1s spectra (Fig. 2b) exhibit a dominant peak at 284.7 eV indicating the presence of graphitic carbon (sp^2 hybridization), as well as peaks corresponding to alcohol or C–*O*–P groups (286.2 eV), carbonyl groups (287.5 eV), and carboxylic or ester groups (289.0 eV) [39]. O 1s XPS spectra (Fig. 2c) reveal peaks characteristic of C═O or P═O bonds (531.2 eV), as well as C–*O*–H or C–*O*–P groups (533.2 eV), and aromatic C–O or P–*O*–P groups at 534.5 eV [40].

The TG plots of the PA-PX_mix samples, and that of Pluronic® F-127 for comparison, are shown in Fig. 3a. Initially, TG analysis of pure phytic acid (PA-P0_mix) reveals a primary mass loss attributed to the elimination of water molecules. Notably, this mass loss persists above 100 °C, reflecting a distinctively strong interaction between water and PA molecules stemming from the initial solution. At 148 °C, a pronounced and abrupt decrease in mass is observed, likely signifying the definitive desorption of water due to the high temperature. Subsequently, at 330 °C, a further mass loss appears, attributed to the dehydration and carbonization processes of PA [41]. Finally, two additional mass losses occur at 650 and 900 °C, indicating structural and chemical modifications within the carbon material, as well as the elimination of phosphorus-derived groups [22].

In contrast, Pluronic® F-127 exhibits a single and complete mass loss detected at 385 °C, denoting its total degradation at this temperature [42]. However, when a range of Pluronic® F-127 quantities is combined with a fixed amount of PA, striking distinctions become evident. In cases where lower amounts of Pluronic® F-127 are employed (PA-P0_mix to PA-P2_mix), the initial mass loss associated with water elimination remains observable. Curiously, this mass loss is absent in the other samples. This phenomenon could be attributed to the abundant presence of Pluronic® F-127 in the initial material, which limits the interaction between water molecules, thus facilitating their desorption at lower temperatures.

Subsequently, a secondary mass loss is discernible in all samples, likely associated with the elimination of Pluronic® F-127, as indicated by the relatively large mass loss. Notably, this mass loss undergoes significant variations between samples PA-P1_mix to PA-P7_mix, deviating considerably from the original Pluronic® F-127. It is striking to note that a direct correlation emerges, namely that the greater the quantity of Pluronic® F-127, the higher the temperature at which its elimination occurs, ranging from 215 °C in PA-P1_mix to 250 °C in PA-P7_mix, thus approaching the initial degradation temperature of Pluronic® F-127 (385 °C). Furthermore, it is noteworthy that the mass loss attributed to Pluronic® F-127 elimination is not complete in any sample, as evidenced by a residual mass lower than the initial amount of Pluronic® F-127 (Table S3). This intriguing phenomenon of decreasing temperature and amount of Pluronic® F-127 removed could be associated with the presence of hydroxyl groups in Pluronic® F-127, which may promote condensation reactions with the phosphate groups of PA, similar to those reported in the activation of cellulose with phosphoric acid [43]. Subsequently, the peak corresponding to the dehydration and carbonization process of PA (at 330 °C) was observed consistently in all samples, albeit with a minor shift towards lower temperatures with increasing Pluronic® F-127 content. Interestingly, the bulk P content of the PA-PX materials generally increases with higher Pluronic® F-127 content, reflecting the enhanced incorporation of phosphate groups during carbonization. However, for the samples with the highest Pluronic® F-127 content (PA-P6 and PA-P7), a slight decrease in bulk P content is observed. This behavior can be attributed to the incomplete elimination of Pluronic® F-127 during pyrolysis. Once the Pluronic® F-127 fraction exceeds that of PA-P5, the amount effectively removed during carbonization reaches a maximum, and further increases in polymer content do not result in proportional elimination. Consequently, the relative fraction of phosphorus incorporated in the final carbon matrix decreases, leading to the observed reduction in bulk phosphorous content for PA-P6 and PA-P7.

Remarkably, the temperature associated with the first peak related to structural and chemical modifications in PA (at 650 °C), previously identified as the elimination of polyphosphate-type groups [22], decreases significantly with higher Pluronic® F-127 content, reaching only 470 °C, while the second peak (at 900 °C) undergoes a marginal decrease. This trend may explain the relatively higher ratio of phosphorous functional groups in the carbon structures (Table 1), despite the increased content of Pluronic® F-127 (not containing P) in the blend. These temperature shifts imply substantial variations in the structural and chemical transformations occurring during the carbonization process of PA, attributed to the different levels of Pluronic® F-127 present in the material. However, NMR results prior to heat treatment (Fig. S5) reveal no differences in the PA-PX_mix series. This suggests that such interactions may occur during the heat treatment process. Indeed, the formation of polyphosphate-type groups could be due to the reaction between the phosphate groups from the starting PA molecules, which are eliminated at 650 °C. It is observed that the mass loss due to the

Table 1
Mass (wt.%) and atomic (at.%) phosphorus (P) contents obtained by CIC and XPS, respectively. Ratio of phosphorus-carbon bonds (P–C) to total phosphorus (P_T) obtained from XPS.

Sample	Bulk P wt.%	Surface P at.%	P–C/P_T ratio
PA-P0	3.1	4.8	0.36
PA-P1	3.2	4.8	0.55
PA-P2	4.3	4.0	0.77
PA-P3	5.3	6.5	0.74
PA-P4	5.0	7.7	0.80
PA-P5	6.0	7.5	0.81
PA-P6	4.8	7.5	0.85
PA-P7	4.9	7.7	0.70

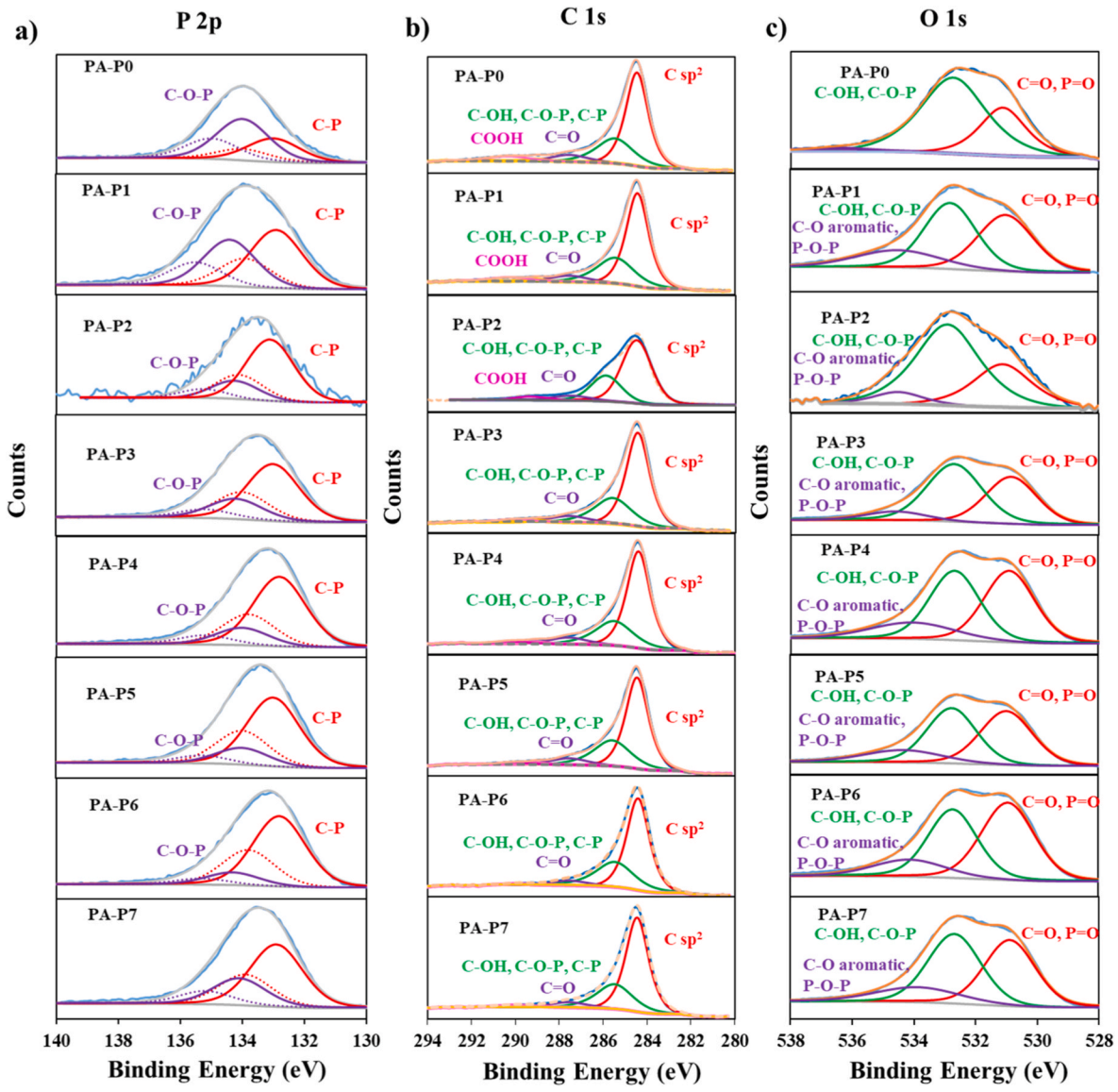

Fig. 2. XPS spectra of P 2p (a), C 1s (b) and O 1s (c) of all PA-PX samples.

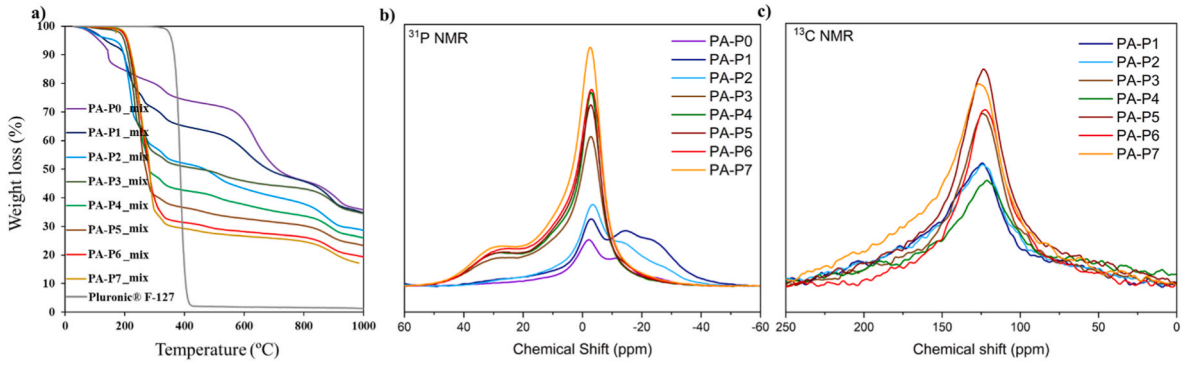

Fig. 3. a) TG plots of PA-PX_mix samples. b) ^{31}P and c) ^{13}C solid-state MAS-NMR spectra of all PA-PX samples.

elimination of polyphosphate-type groups at this temperature decreases when Pluronic® F-127 is added in the mechanosynthesis step. The addition of Pluronic® F-127 could reduce the interactions between PA molecules, thereby generating fewer and shorter polyphosphate-type groups, shifting their elimination to lower temperatures and reducing mass loss.

To complement the interpretation of the thermogravimetric data, the carbonization yield was determined from the TG curves after excluding the initial mass loss associated with water evaporation from the PA solution, as this process does not contribute to carbon formation. The

precursor containing only PA (PA-P0_mix) displays a carbonization yield of approximately 50%, consistent with the expected residual mass after PA dehydration and carbonization. Importantly, the carbonaceous fraction in the final materials originates from both PA and the fraction of Pluronic® F-127 that is not completely decomposed during pyrolysis, despite its primary role as a soft template. As the amount of Pluronic® F-127 increases in the precursor mixtures, the overall carbonization yield progressively decreases, from about 50% down to approximately 20%, due to the increasing proportion of template in the initial composition.

The ^{31}P-MAS-NMR spectra of the phosphorous doped carbons (Fig. 3b) immediately reveal two clear trends. Firstly, absolute signal intensities indicate more successful P incorporation from PA-P3 onward (as spectral acquisition times were held constant), evidencing the crucial interaction of Pluronic® F-127 in the phosphorous doping mechanism and confirming the upward trend in P incorporation shown in Table 1. Secondly, a systematic evolution of the dominant chemical shifts can be noted: whereas PA-P1 and PA-P2 exhibit an upfield shoulder with two maximum contributions at −13 ppm and −24 ppm, this chemical environment disappears when more Pluronic® F-127 is incorporated. On the other hand, a pronounced contribution around 25 ppm arises from PA-P3. We can therefore deduce that the P environments undergo a gradual change depending on their interaction with Pluronic® F-127. The environment observed at −24 ppm and −13 ppm is typically assigned to polyphosphate and pyrophosphate groups respectively, whose formation can be rationalized due to the relatively high P content of PA. By further increasing the Pluronic® F-127 content, the phosphate moieties are initially more 'diluted' in the sample, reducing the chances of a direct interaction, as also shown by the TG plots discussed above. The broad shoulder spanning chemical shifts between 35 and 15 ppm is assigned to the presence of aryl-substituted organophosphonate species and, to a more limited extent, phosphonic acid anhydrides (confirmed by theoretical simulations, see below), resulting from thermally induced interaction between phosphate groups and Pluronic® F-127.

The main signal at −2.5 ppm exhibits a high degree of asymmetry, indicating that it is in fact the envelope of multiple environments. To get an idea of the constituent contributions, the corresponding CP-MAS ^{31}P NMR spectra were collected (Fig. S6a), as well as a superposition of the PA-P7 MAS and CP-MAS ^{31}P NMR spectrum (Fig. S6b). It is immediately noticeable that the relative intensity of the main signal (−2.5 ppm) with respect to the broad 15-35 ppm shoulder, assigned to phosphonate species, decreases sharply in the CP-MAS. This indicates that a significant contribution from the most intense peak can be partly attributed to a proton-poor environment, such as the triphenylphosphine environment where the P heteroatom is fully incorporated into graphitic sheets. In addition, the shift of the peak maximum to 4 ppm in the CP-MAS can explain the asymmetry of the MAS signal, signifying that another, more proton-rich and flexible P environment is superimposed. Given the range of chemical shifts, aryl-substituted phosphate esters can also be expected. The pronounced amplification of functional groups with direct P–C bonds when the PA-P2 ratio is exceeded is in line with the XPS results already presented in Table 1.

Fig. 3c presents the ^{13}C-solid-state MAS-NMR spectra for the PA-PX series. Across all samples, a broad peak is observed within the 127-130 ppm range, which is indicative of conjugated sp^2 bonds commonly found in condensed aromatic structures, as inferred earlier from XRD and Raman spectroscopy analyses.

To support the band assignment in the ^{31}P NMR spectra, the ^{31}P NMR shifts of six periodic models were calculated using periodic Density Functional Theory (DFT) (see Fig. 6a). The models are based on experimental results and structural motifs proposed in previous work [26], where, for simplicity, graphene sheets were used. Four structures feature the P substitution at the edges of zigzag hydrogen-terminated graphene. Structures PC_1 and PC_2 are organophosphonic with P–C bonds, showing substitution by phosphonic acid (PC_1) and phosphonic acid anhydride (PC_2). Structures PO_1 and PO_2, on the other hand, are phosphate-type, *i.e* with C–*O*–P bonds, and feature substitution by phosphoric acid monoester and diester. For PC_1 and PO_1, conformational searches were carried out, and the results discussed here correspond to the lowest-energy conformers (see Fig. S7 and Table S4 for details). We also considered two models derived from a graphene sheet with phosphine- (PG_1) and phosphine-oxide (PG_2) substitution. The computational approach was validated by calculating the ^{31}P NMR shifts of five molecular analogues with the same method and comparing them with reference values. The calculated shifts are presented in Table S4.

In the calculations, phosphonic-type edge substituents have positive shifts (33 and 11 ppm for models PC_1 and PC_2), and phosphoric-type substituents have negative shifts (−19 and −17 ppm for models PO_1 and PO_2), in agreement with the assignment of the experimental bands proposed above (see again Table S4). Furthermore, the phosphine-like substitution has a shift of −6 ppm (model PG_1), which is also within the range of observed shifts (see Fig. 3b). However, the phosphine oxide analogue (model PG_2) has a shift of −41 ppm which is not observed experimentally, suggesting that incorporated phosphine oxide species are not significant in the samples.

According to all characterization results, the reduced formation of polyphosphate chains during the synthesis process of phosphorous doped carbons, conditioned by the presence of Pluronic® F-127, leads to different consequences illustrated in Fig. 4.

These mechanisms are: 1) The formation of fewer or shorter polyphosphate chains leads to the production of materials with less porosity and lower A_{BET}, since porosity could be produced mainly by the elimination of such chains. 2) The higher amount of Pluronic® F-127 results in a greater initial distribution of phosphate groups, which are likely to be transformed into phosphonic-type or phosphine-like species during heat treatment, while preserving a higher P content (see Fig. 4).

3.3. Electrochemical performance

Electrochemical performance towards HER was measured for all phosphorous doped materials. Before evaluating the electrocatalytic performance, the electrochemical stability of the PA-P6, used as representative sample, was examined by cyclic voltammetry in acidic medium (Fig. S8). The voltammograms recorded prior to HER testing showed no redox peaks, indicating that the phosphorus-containing surface groups remain electrochemically stable within the applied potential window. To assess their electrocatalytic capability, the phosphorous doped carbons were subjected to linear sweep voltammetry (LSV) in an N_2-saturated acidic electrolyte (0.5 M H_2SO_4), and the results are depicted in Fig. 5a and b. Notably, the greater the quantity of Pluronic® F-127, the lower the overpotential for HER (E_{HER}), signifying improved electrocatalytic performance. This improvement in electrocatalytic efficiency reaches its maximum in PA-P6, with an outstanding E_{HER} of −0.19 V vs. RHE. In the absence of Pluronic® F-127 (PA-P0), however, the material exhibits negligible electrocatalytic activity.

The determination of Tafel slopes provides crucial insights into the rate-determining step, shedding light on the diversity of active sites within these materials. The two commonly accepted pathways, Volmer-Tafel and Volmer-Heyrovsky, are described as follows:

$$H_2O + e^- \longrightarrow H_{ads} + OH^- \text{ (Volmer) (1)}$$

$$H_{ads} + H_3O^+ + e^- \longrightarrow H_2 + H_2O \text{ (Heyrovsky) (2)}$$

$$H_{ads} + H_{ads} \longrightarrow H_2 \text{ (Tafel)} \quad (3)$$

Fig. 5c illustrates the Tafel slopes for HER in the 0.5 M H_2SO_4 solution. For all materials, Tafel slopes range from −113 to −192 mV dec^{-1}, except for PA-P0 and PA-P1, where notably more negative slopes are observed. Tafel slopes around −120 mV dec^{-1} are related to the Volmer rate-determining step, or alternatively, to the Heyrovsky rate-determining step with high coverage of adsorbed hydrogen atoms [44]. However, the disparity of Tafel slopes observed suggests that different HER mechanisms are involved, depending on the different P

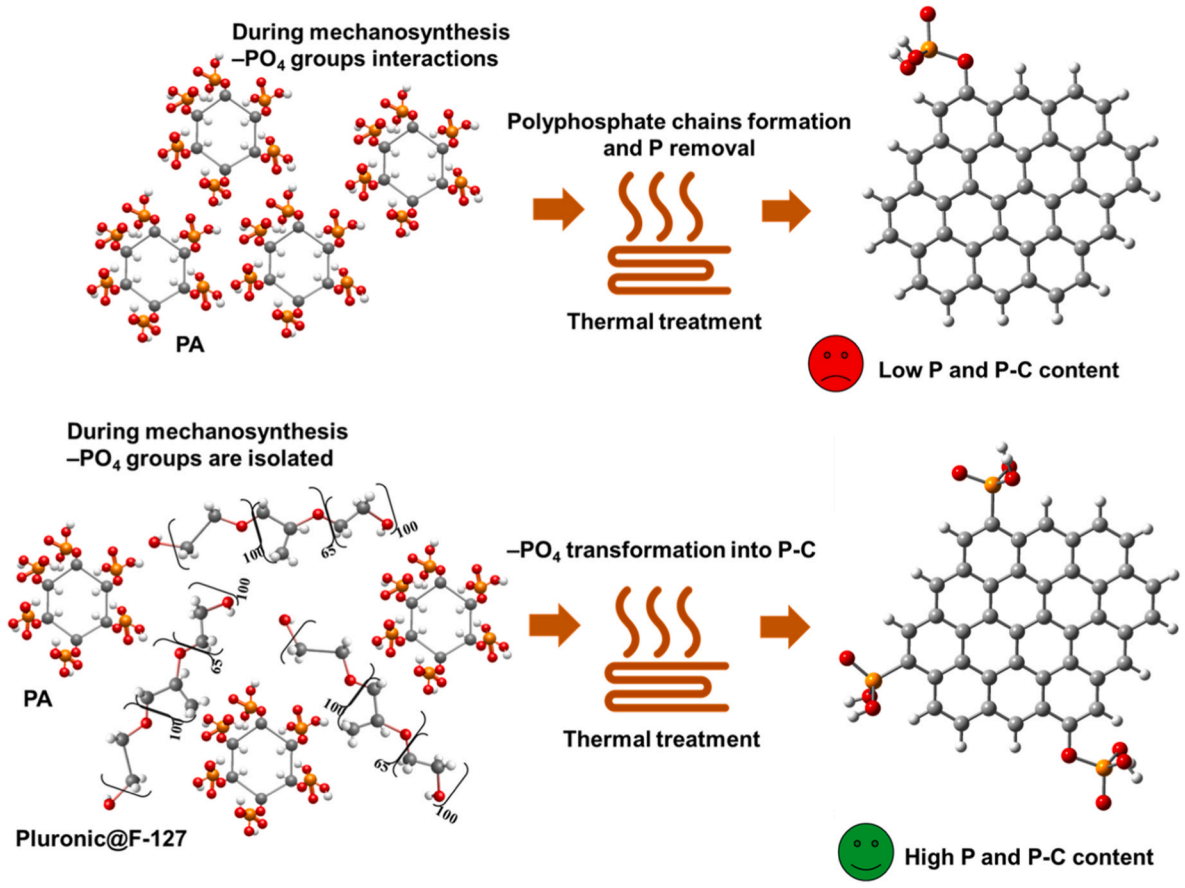

Fig. 4. Schematic representation of the influence of Pluronic® F-127 in the synthesis of phosphorous doped carbons.

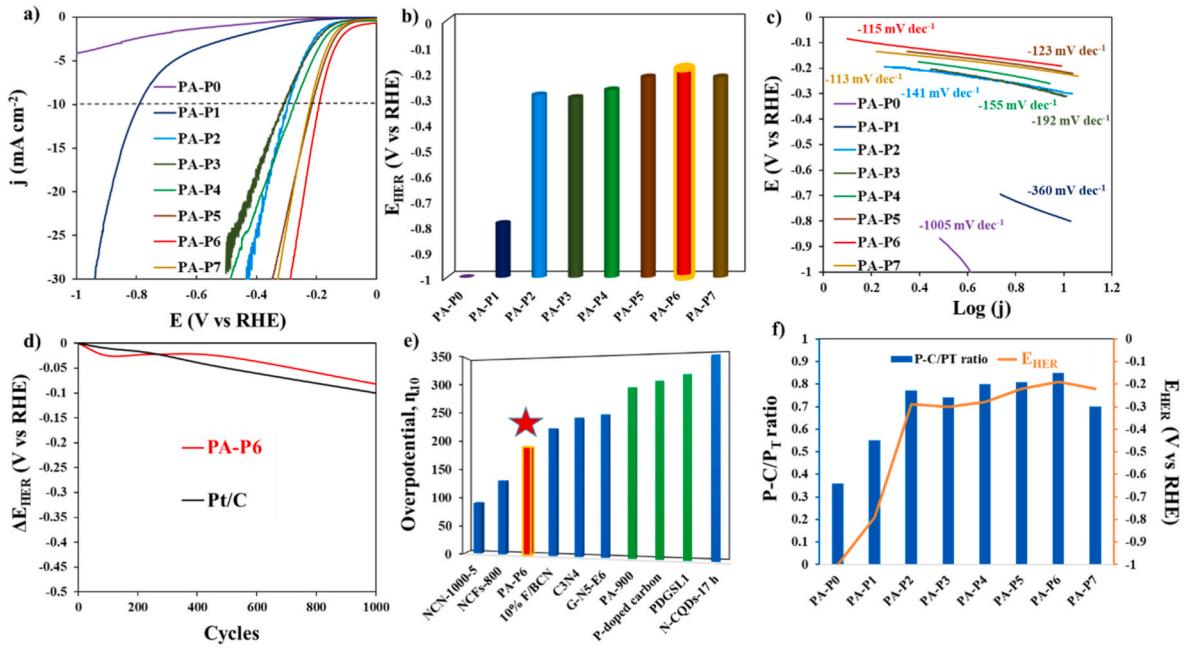

Fig. 5. a) Linear sweep voltammetry and b) graphical representation of E_{HER} values in a 0.5 M H_2SO_4, N_2-saturated solution at 50 mV s^{-1} of the as-prepared materials. c) Tafel slopes of all synthesized samples. d) Stability study of variation in E_{HER} values of PA-P6 and commercial Pt/C. e) Literature comparison of HER performance of metal-free materials (blue for N-doped carbons and green for phosphorous doped carbons) with PA-P6 (red). f) Graphical representation of P–C bonds/P_T atomic ratio (blue bars) and E_{HER} values (orange line) of the entire PA-PX series. (For interpretation of the references to colour in this figure legend, the reader is referred to the Web version of this article.)

species determined. Remarkably, the phosphorous doped carbons synthesized with the highest Pluronic® F-127 content exhibit the most

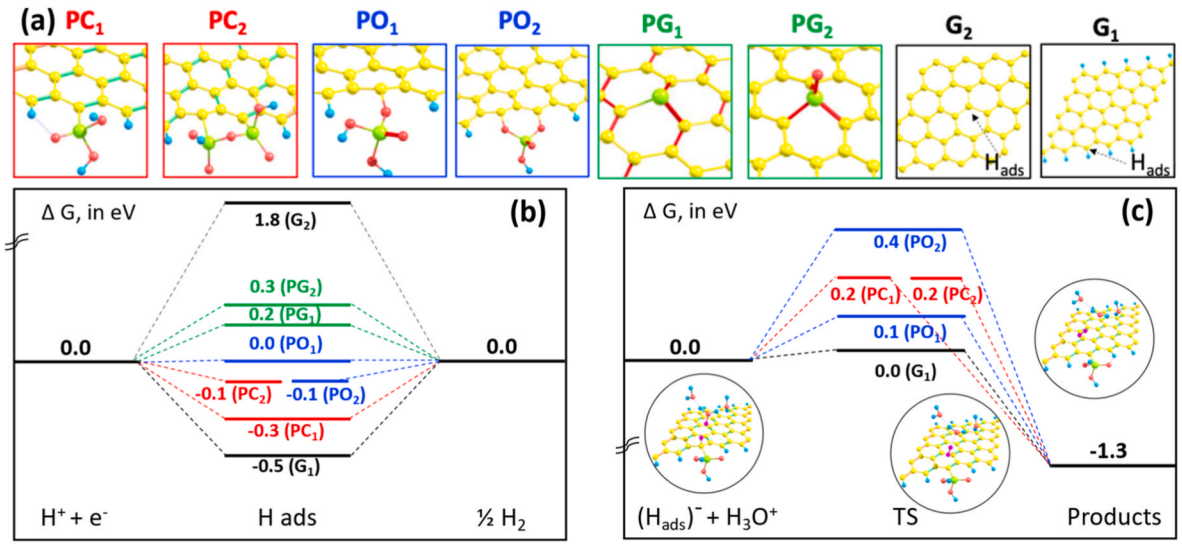

Fig. 6. (a) Representation of simulated, periodic phosphorous doped and non-doped graphene models. Free energy profiles for (b) Volmer and (c) Heyrovsky mechanisms.

positive Tafel slopes.

Moreover, the similar Tafel plots observed for materials obtained with a higher Pluronic® F-127 content (PA-P5, PA-P6 and PA-P7) imply the presence of similar active sites. Furthermore, the stability of the most efficient electrocatalyst, PA-P6, was subjected to rigorous testing under operational conditions, involving 1000 consecutive LSV cycles, as shown in Fig. 5d. Impressively, this material exhibits outstanding stability over multiple cycling sessions. Although a slight decrease in stability is observed after the first 200 cycles, it then reaches a plateau and retains its robust stability even after the full 1000 cycles. This level of stability notably surpasses that of the commercial Pt/C catalyst, a benchmark material in this field. To further evaluate the structural stability of the catalysts during the HER, cyclic voltammetry (CV) measurements were performed before and after the electrolysis. Despite the high current densities applied during the HER, the PA-P6 catalyst exhibits only a slight decrease in double-layer capacitance, while maintaining the quasi-rectangular CV profile characteristic of carbon-based materials (Fig. S8). This indicates that the overall conductive carbon network remains largely intact and that the surface area accessible to the electrolyte is only minimally affected. The minor decrease in capacitance can be attributed to subtle changes at the carbon–electrolyte interface, likely involving partial reorganization or minor loss of labile phosphate groups that do not disrupt the main conductive framework. Importantly, the retention of the characteristic CV shape suggests that the P–C-type species responsible for HER activity are preserved throughout the reaction, supporting the excellent durability observed for the catalyst. These results highlight that, although minor surface modifications may occur, the intrinsic active sites and structural features crucial for hydrogen evolution remain stable under prolonged electrochemical operation.

The exceptional electrochemical performance and remarkable stability demonstrated by PA-P6 underscore its potential as a highly promising metal-free carbon-based electrocatalyst for the HER. These findings further reinforce the viability of PA-derived carbon materials as efficient and stable HER electrocatalysts, with the potential to advance sustainable hydrogen production technologies.

It is noteworthy that the PA-P6 catalyst performs competitively with the leading metal-free electrocatalysts reported in the literature (Fig. 5e and Table S5) [16,21,23,26,45–49]. The electrocatalytic activity of PA-P6 exceeds that of the best-performing phosphorous doped materials documented to date, demonstrating significant superiority. Furthermore, PA-P6 also shows competitive activity with N-doped materials. Importantly, these results are increasingly approaching the performance of noble-metal-based catalysts, such as commercial Pt/C, which delivers an overpotential of −38 mV at −10 mA cm^{-2}, highlighting the promise of phosphorous doped carbons as efficient and sustainable metal-free HER electrocatalysts.

The textural and structural properties of the PA-PX materials are expected to influence their electrocatalytic performance. As the Pluronic® F-127 content increases, a decrease in surface area and pore volume is observed, which could, in principle, limit the accessibility of active sites and hinder electrolyte transport. At the same time, XRD and Raman analyses indicate that higher Pluronic® F-127 contents promote the formation of more graphitic domains, enhancing the electrical conductivity of the materials and facilitating charge transfer during HER. These results suggest that while surface area, porosity, and carbon ordering contribute to the catalytic performance, they are not the sole determinants; the chemical nature and availability of active phosphorus sites remain critical for achieving high HER activity.

In order to relate phosphorus nature with its electrocatalytic activity, the ratio of P–C-type species (P–C) to total phosphorus (P_T) obtained from XPS (see again Table 1), as well as the E_{HER} vs RHE performance of each sample are represented in Fig. 5f. A closer comparison between PA-P1 and PA-P2 highlights that, despite exhibiting very similar textural and structural properties, their catalytic activity towards HER differs drastically. This discrepancy can be attributed to the marked increase in the P–C/P_T ratio observed by XPS when moving from PA-P1 to PA-P2, which correlates with the improvement in catalytic activity. Interestingly, the highest HER catalytic performance was obtained with carbons prepared with the highest Pluronic® F-127 content, which is in agreement with the largest value of P–C/P_T ratio. According to previous work, the content of P–C-type species plays a key role in the electrochemical activity of HER [26]. These results reinforce the crucial role of P–C moieties as the main active sites in phosphorous doped carbons, beyond purely textural or structural effects.

3.4. *Theoretical calculations*

To elucidate the mechanism of electrocatalytic water reduction in experimental systems and clarify the effect of P doping, DFT calculations for the Volmer-Heyrovsky and Volmer-Tafel mechanisms have been carried out for model systems (Fig. 6a) using the computational hydrogen electrode approach (see experimental section for details) [50]. Graphene edge (thus 1D) (G1) and pristine graphene sheet (thus 2D)

(G2) are considered as references.

From the different tests, the results for the adsorption of a single hydrogen atom (Volmer step) on the most favorable sites are shown in Fig. 6b. In the edge models PC_n and PO_n, adsorption occurs preferentially at the edge carbons bearing the P or O substituent, where the models also exhibit the highest spin density prior to adsorption (see Fig. S9). In the embedded P models, the preferred H absorption sites are the P atom (model PG_1) and one of the C atoms attached to the P atom (model PG_2). This preference dictated by spin density is in line with previous results correlating the density of states (DOS) on the surface active center with the H adsorption strength in heteroatom-doped graphene [51]. Energetically, H adsorption energies range from −0.3 to 0.3 eV, with a negative value indicating an exergonic step. The organophosphonic models PC_1 and PC_2 have the most favorable adsorption, −0.3 eV and −0.1 eV. The affinity of the phosphorous substituted models lies between graphene edge (G1), which has the highest affinity (−0.5 eV), and graphene sheet (G2), which has the lowest one (1.8 eV).

The Heyrovsky step (see Fig. 6c) has been modeled by calculating the reaction between the reduced surface with an adsorbed H atom (*i.e*, H_{ads} plus one e^-) and a hydronium ion clustered with two other water molecules (see Experimental Section). The reaction coordinates show low barriers of 0.1 - 0.2 eV for models PC_1, PC_2 and PO_1, and a higher barrier of 0.4 eV for PO_2. By comparison, this step is almost barrier-free in PG_1, PG_2, G1 and G2. These barriers are significantly lower than those reported for the same step on an N-doped carbon nanotube [52]. The results show that the Volmer-Heyrovsky mechanism is energetically favorable for the phosphorous doped graphene-based models, since it is associated with barriers of 0.6 eV or less, and for G1. In contrast, the Tafel mechanism is less favorable (see Fig. S10). In this mechanism, the adsorption of a second H atom is less favorable than the first one, and requires a free energy of 0.5 - 1.1 eV H_2 elimination requires an additional barrier, bringing the overall free energy required to about 2 eV. The Volmer-Tafel energy profiles agree with previous studies of graphene-based systems [51,53,54].

Overall, DFT calculations suggest that substitution of graphene edges with organophosphonic and phosphoric acid residues should lead to good electrocatalytic activity for hydrogen evolution in acidic media, following the Volmer-Heyrovsky mechanism. It can be assumed that this also applies to graphitic systems. Therefore, the calculations provide insights into the P incorporation patterns that might be responsible for the electrocatalytic activity in the synthesized materials. In particular, the favorable Volmer-Heyrovsky energy profile for PC_1 and PC_2 is consistent with the key role of P–C-containing species suggested by the electrochemical experiments.

The experimental and computational results consistently indicate that P–C-type moieties are the main active sites for HER in our phosphorous doped carbon materials. DFT calculations show that moderately favorable proton adsorption, as observed for the PC2 and PO2 configurations, enables efficient reaction progression in the Volmer step while avoiding overly strong binding, as seen in PC1 and G configurations, which could hinder proton desorption in the subsequent Heyrovsky step. Although PO1 shows slightly more favorable energetics in the second step, the overall reaction is dominated by the Volmer step, making PC2 the globally optimal configuration. This explains why samples with higher P–C content exhibit superior HER performance, highlighting the critical role of controlling surface phosphorus chemistry to optimize metal-free electrocatalytic activity.

4. Conclusions

This study highlights the underexplored potential of precisely modulating phosphorus species and physicochemical properties of metal-free carbons to enhance their electrocatalytic performance in the hydrogen evolution reaction (HER). Beyond their conventional roles in controlling particle size and pore structure, surfactants, particularly Pluronic® F-127, emerge as critical agents for surface chemistry modification. Pluronic® F-127 functions as a "diluting" agent during the pyrolysis of PA, effectively preventing the aggregation of phosphorus groups. This mechanism inhibits the formation of polyphosphoric species, instead favoring the incorporation of isolated P functionalities into the carbon basal planes. Comprehensive characterization, supported by DFT simulations, revealed the precise nature of the phosphorus species in the materials, demonstrating how their fine-tuning results in exceptional catalytic activity. The optimized phosphorous doped carbon electrocatalyst achieved state-of-the-art HER performance (E_{HER} = −0.19 vs. RHE), without the need for metal catalysts. This study opens new avenues for the rational design of advanced metal-free electrocatalysts, paving the way for innovations in sustainable hydrogen production technologies.

CRediT authorship contribution statement

Sergio García-Dalí: Writing – review & editing, Writing – original draft, Investigation, Conceptualization. **Javier Quílez-Bermejo:** Writing – review & editing, Investigation. **Denis Diatlov:** Writing – review & editing, Formal analysis. **Wouter Marchal:** Writing – review & editing, Formal analysis. **Elien Derveaux:** Writing – review & editing, Formal analysis. **Jimena Castro-Gutiérrez:** Writing – review & editing, Formal analysis. **María T. Izquierdo:** Writing – review & editing, Formal analysis. **Lluís Blancafort:** Writing – review & editing, Supervision, Funding acquisition, Formal analysis. **Alain Celzard:** Writing – review & editing, Supervision, Funding acquisition, Formal analysis. **Vanessa Fierro:** Writing – review & editing, Supervision, Funding acquisition.

Data availability

The data that support the findings of this study are available within the article and Supplementary Information.

Declaration of competing interest

The authors declare that they have no known competing financial interests or personal relationships that could have appeared to influence the work reported in this paper.

Acknowledgments

This study was partly supported by the French PIA project "Lorraine Université d'Excellence", reference ANR-15-IDEX-04-LUE, and the TALiSMAN project funded by ERDF (2019-000214). SGD thanks the Ministerio de Universidades, the European Union and the University of Oviedo for their financial support (MU-21-UP2021-030 30267158). L. B. and D. D. acknowledge financial support by projects PID2022-138062NB-I00 and PRE2020-093504 from Ministerio de Ciencia e Innovación, Spain, and computational time from Red Española de Supercomputación, project QHS-2024-1-0031, and Consorci de Serveis Universitaris de Catalunya.

Appendix A. Supplementary data

Supplementary data to this article can be found online at https://doi.org/10.1016/j.carbon.2026.121425.

References

[1] J. Zhu, L. Hu, P. Zhao, L.Y.S. Lee, K.Y. Wong, Recent advances in electrocatalytic hydrogen evolution using nanoparticles, Chem. Rev. 120 (2020) 851–918, https://doi.org/10.1021/acs.chemrev.9b00248.

[2] F. Cheng, J. Chen, Metal–air batteries: from oxygen reduction electrochemistry to cathode catalysts, Chem. Soc. Rev. (2012) 2172–2192, https://doi.org/10.1039/c1cs15228a.

[3] Z.-L. Wang, D. Xu, J.-J. Xu, X.-B. Zhang, Oxygen electrocatalysts in metal–air batteries: from aqueous to nonaqueous electrolytes, Chem. Soc. Rev. 43 (2013) 7746–7786, https://doi.org/10.1039/c3cs60248f.
[4] J. Stacy, Y.N. Regmi, B. Leonard, M. Fan, The recent progress and future of oxygen reduction reaction catalysis: a review, Renew. Sustain. Energy Rev. 69 (2017) 401–414, https://doi.org/10.1016/j.rser.2016.09.135.
[5] A. Morozan, B. Jousselme, S. Palacin, Low-platinum and platinum-free catalysts for the oxygen reduction reaction at fuel cell cathodes, Energy Environ. Sci. 4 (2011) 1238–1254, https://doi.org/10.1039/c0ee00601g.
[6] E.J. Popczun, C.G. Read, C.W. Roske, N.S. Lewis, R.E. Schaak, Highly active electrocatalysis of the hydrogen evolution reaction by cobalt phosphide nanoparticles, Angew. Chem. (2014) 5531–5534, https://doi.org/10.1002/ange.201402646.
[7] B. Hinnemann, P.G. Moses, J. Bonde, K.P. Jørgensen, J.H. Nielsen, S. Horch, I. Chorkendorff, J.K. Nørskov, Biomimetic hydrogen evolution : MoS2 nanoparticles as catalyst for hydrogen evolution, J. Am. Chem. Soc. (2005) 5308–5309, https://doi.org/10.1021/ja0504690.
[8] H. Li, Q. Li, P. Wen, T.B. Williams, S. Adhikari, C. Dun, C. Lu, D. Itanze, L. Jiang, D. L. Carroll, G.L. Donati, P.M. Lundin, Y. Qiu, S.M. Geyer, Colloidal cobalt phosphide nanocrystals as trifunctional electrocatalysts for overall water splitting powered by a zinc–air battery, Adv. Mater. 30 (2018) 1705796, https://doi.org/10.1002/adma.201705796.
[9] L. Tian, X. Yan, X. Chen, Electrochemical activity of iron phosphide nanoparticles in hydrogen evolution reaction, ACS Catal. 6 (2016) 5441–5448, https://doi.org/10.1021/acscatal.6b01515.
[10] J. Masa, W. Xia, M. Muhler, W. Schuhmann, On the role of metals in nitrogen-doped carbon electrocatalysts for oxygen reduction, Angew. Chem., Int. Ed. 54 (2015) 10102–10120, https://doi.org/10.1002/anie.201500569.
[11] K. Zhang, Y. Zhang, Q. Zhang, Z. Liang, L. Gu, W. Guo, B. Zhu, S. Guo, R. Zou, Metal-organic framework-derived Fe/Cu-substituted Co nanoparticles embedded in CNTs-grafted carbon polyhedron for Zn-air batteries, Carbon Energy 2 (2020) 283–293, https://doi.org/10.1002/cey2.35.
[12] S. Li, C. Cheng, X. Zhao, J. Schmidt, A. Thomas, Active Salt/Silica-Templated 2D mesoporous FeCo-Nx-Carbon as bifunctional oxygen electrodes for zinc-air batteries, Angew. Chem., Int. Ed. 57 (2018) 1856–1862, https://doi.org/10.1002/anie.201710852.
[13] J. Quílez-Bermejo, S. García-Dalí, A. Daouli, A. Zitolo, R.L.S. Canevesi, M. Emo, M. T. Izquierdo, M. Badawi, A. Celzard, V. Fierro, Advanced design of metal nanoclusters and single atoms embedded in C1N1-Derived carbon materials for ORR, HER, and OER, Adv. Funct. Mater. (2023) 2300405, https://doi.org/10.1002/adfm.202300405.
[14] C. Hu, H. Liu, Y. Liu, J.F. Chen, Y. Li, L. Dai, Graphdiyne with tunable activity towards hydrogen evolution reaction, Nano Energy 63 (2019) 103874, https://doi.org/10.1016/j.nanoen.2019.103874.
[15] S. Li, Z. Yu, Y. Yang, Y. Liu, H. Zou, H. Yang, J. Jin, J. Ma, Nitrogen-doped truncated carbon nanotubes inserted into nitrogen-doped graphene nanosheets with a sandwich structure: a highly efficient metal-free catalyst for the HER, J. Mater. Chem. A 5 (2017) 6405–6410, https://doi.org/10.1039/C7TA00961E.
[16] J. Sun, Q. Ge, L. Guo, Z. Yang, Nitrogen doped carbon fibers derived from carbonization of electrospun polyacrylonitrile as efficient metal-free HER electrocatalyst, Int. J. Hydrogen Energy 45 (2020) 4035–4042, https://doi.org/10.1016/j.ijhydene.2019.11.204.
[17] J. Quílez-Bermejo, M. Melle-Franco, E. San-Fabián, E. Morallón, D. Cazorla-Amorós, Towards understanding the active sites for the ORR in N-doped carbon materials through fine-tuning of nitrogen functionalities: an experimental and computational approach, J. Mater. Chem. A 7 (2019) 24239–24250, https://doi.org/10.1039/C9TA07932G.
[18] D. Guo, R. Shibuya, C. Akiba, S. Saji, T. Kondo, J. Nakamura, Active sites of nitrogen-doped carbon materials for oxygen reduction reaction clarified using model catalysts, Science 351 (2016) 361–365, https://doi.org/10.1126/science.aad0832.
[19] K. Gong, F. Du, Z. Xia, M. Durstock, L. Dai, Nitrogen-Doped carbon nanotube arrays with high electrocatalytic activity for oxygen reduction, Science 323 (2009) 760–764, https://doi.org/10.1126/science.1168049.
[20] W. Ding, Z. Wei, S. Chen, X. Qi, T. Yang, J. Hu, D. Wang, L. Wan, S.F. Alvi, L. Li, Space-Confinement-Induced synthesis of pyridinic- and pyrrolic-nitrogen-doped graphene for the catalysis of oxygen reduction, Angew. Chem. Int. Ed. 52 (2013) 11755–11759, https://doi.org/10.1002/anie.201303924.
[21] Z. Liu, J. Ai, M. Sun, F. Han, Z. Li, Q. Peng, Q. Wang, J. Liu, L. Liu, Phosphorous-Doped graphite layers with outstanding electrocatalytic activities for the oxygen and hydrogen evolution reactions in water electrolysis, Adv. Funct. Mater. 30 (2020) 1910741, https://doi.org/10.1002/adfm.201910741.
[22] S. García-Dalí, J. Quílez-Bermejo, J. Castro-Gutiérrez, N. Baccile, M.T. Izquierdo, A. Celzard, V. Fierro, Green and easy synthesis of P-doped carbon-based hydrogen evolution reaction electrocatalysts, Carbon 212 (2023), https://doi.org/10.1016/j.carbon.2023.118154.
[23] J. Zhao, Z. Pu, H. Jin, Z. Zhang, J. Liu, S. Mu, Phosphorous-doped carbon coordinated iridium diphosphide bifunctional catalyst with ultralow iridium amount for efficient all-ph-value hydrogen evolution and oxygen reduction reactions, J. Catal. 383 (2020) 244–253, https://doi.org/10.1016/j.jcat.2020.01.026.
[24] Y. Lei, M. Jia, P. Guo, J. Liu, J. Zhai, MoP nanoparticles encapsulated in P-doped carbon as an efficient electrocatalyst for the hydrogen evolution reaction, Catal. Commun. 140 (2020) 106000, https://doi.org/10.1016/j.catcom.2020.106000.
[25] J. Castro-Gutiérrez, A. Sanchez-Sanchez, J. Ghanbaja, N. Díez, M. Sevilla, A. Celzard, V. Fierro, Synthesis of perfectly ordered mesoporous carbons by water-assisted mechanochemical self-assembly of tannin, Green Chem. 20 (2018) 5123–5132, https://doi.org/10.1039/C8GC02295J.
[26] S. García-Dalí, J. Quílez-Bermejo, J. Castro-Gutiérrez, N. Baccile, M.T. Izquierdo, A. Celzard, V. Fierro, Green and easy synthesis of P-doped carbon-based hydrogen evolution reaction electrocatalysts, Carbon 212 (2023) 118154, https://doi.org/10.1016/j.carbon.2023.118154.
[27] M. Thommes, K. Kaneko, A.V. Neimark, J.P. Olivier, F. Rodriguez-Reinoso, J. Rouquerol, K.S.W. Sing, Physisorption of gases, with special reference to the evaluation of surface area and pore size distribution (IUPAC Technical Report), Pure Appl. Chem. 87 (2015) 1051–1069, https://doi.org/10.1515/pac-2014-1117.
[28] P. Mallet-Ladeira, P. Puech, C. Toulouse, M. Cazayous, N. Ratel-Ramond, P. Weisbecker, G.L. Vignoles, M. Monthioux, A Raman study to obtain crystallite size of carbon materials: a better alternative to the Tuinstra–Koenig law, Carbon 80 (2014) 629–639, https://doi.org/10.1016/j.carbon.2014.09.006.
[29] L. Bouleau, S. Pérez-Rodríguez, J. Quílez-Bermejo, M.T. Izquierdo, F. Xu, V. Fierro, A. Celzard, Best practices for ORR performance evaluation of metal-free porous carbon electrocatalysts, Carbon 189 (2022) 349–361, https://doi.org/10.1016/j.carbon.2021.12.078.
[30] J. Hafner, *Ab-initio* simulations of materials using VASP: density-functional theory and beyond, J. Comput. Chem. 29 (2008) 2044–2078, https://doi.org/10.1002/jcc.21057.
[31] J. Albero, A. Vidal, A. Migani, P. Concepción, L. Blancafort, H. García, Phosphorus-Doped graphene as a metal-free material for thermochemical water reforming at unusually mild conditions, ACS Sustainable Chem. Eng. 7 (2019) 838–846, https://doi.org/10.1021/acssuschemeng.8b04462.
[32] J.K. Nørskov, T. Bligaard, A. Logadottir, J.R. Kitchin, J.G. Chen, S. Pandelov, U. Stimming, Trends in the exchange Current for hydrogen evolution, J. Electrochem. Soc. 152 (2005) J23, https://doi.org/10.1149/1.1856988.
[33] X. Chen, C. Liu, Y. Fang, X. Ai, F. Zhong, H. Yang, Y. Cao, Understanding of the sodium storage mechanism in hard carbon anodes, Carbon Energy 4 (2022) 1133–1150, https://doi.org/10.1002/cey2.196.
[34] M. Okamura, A. Takagaki, M. Toda, J.N. Kondo, K. Domen, T. Tatsumi, M. Hara, S. Hayashi, Acid-catalyzed reactions on flexible polycyclic aromatic carbon in amorphous carbon, Chem. Mater. 18 (2006) 3039–3045, https://doi.org/10.1021/cm0605623.
[35] S. Bernard, O. Beyssac, K. Benzerara, N. Findling, G. Tzvetkov, G.E. Brown, XANES, Raman and XRD study of anthracene-based cokes and saccharose-based chars submitted to high-temperature pyrolysis, Carbon 48 (2010) 2506–2516, https://doi.org/10.1016/j.carbon.2010.03.024.
[36] A.C. Ferrari, J. Robertson, Interpretation of Raman spectra of disordered and amorphous carbon, Phys. Rev. B 61 (2000) 14095–14107, https://doi.org/10.1103/PhysRevB.61.14095.
[37] A.C. Ferrari, J. Robertson, Raman spectroscopy of amorphous, nanostructured, diamond–like carbon, and nanodiamond, Philos. Trans. R. Soc. London, Ser. A: Math. Phys. Eng. Sci. 362 (2004) 2477–2512, https://doi.org/10.1098/rsta.2004.1452.
[38] X. Wu, L.R. Radovic, Inhibition of catalytic oxidation of carbon/carbon composites by phosphorus, Carbon 44 (2006) 141–151, https://doi.org/10.1016/j.carbon.2005.06.038.
[39] J. Xu, L. Chen, H. Qu, Y. Jiao, J. Xie, G. Xing, Preparation and characterization of activated carbon from reedy grass leaves by chemical activation with H 3 PO 4, Appl. Surf. Sci. 320 (2014) 674–680, https://doi.org/10.1016/j.apsusc.2014.08.178.
[40] V. Sydorchuk, O.I. Poddubnaya, M.M. Tsyba, O. Zakutevskyy, O. Khyzhun, S. Khalameida, A.M. Puziy, Photocatalytic degradation of dyes using phosphorus-containing activated carbons, Appl. Surf. Sci. 535 (2021) 147667, https://doi.org/10.1016/j.apsusc.2020.147667.
[41] A.L.M. Daneluti, J. do R. Matos, Study of thermal behavior of phytic acid, Brazilian Journal of Pharmaceutical Sciences 49 (2013) 275–283, https://doi.org/10.1590/S1984-82502013000200009.
[42] G.A. Naikoo, M. Thomas, M. Anis Ganaie, M.U.D. Sheikh, M. Bano, I.U. Hassan, F. Khan, Hierarchically macroporous silver monoliths using Pluronic F127: facile synthesis, characterization and its application as an efficient biomaterial for pathogens, J. Saudi Chem. Soc. 20 (2016) 237–244, https://doi.org/10.1016/j.jscs.2015.12.002.
[43] M. Jagtoyen, F. Derbyshire, Activated carbons from yellow poplar and white oak by H3PO4 activation, Carbon 36 (1998) 1085–1097, https://doi.org/10.1016/S0008-6223(98)00082-7.
[44] T. Shinagawa, A.T. Garcia-Esparza, K. Takanabe, Insight on Tafel slopes from a microkinetic analysis of aqueous electrocatalysis for energy conversion, Sci. Rep. 5 (2015) 13801, https://doi.org/10.1038/srep13801.
[45] H. Jiang, J. Gu, X. Zheng, M. Liu, X. Qiu, L. Wang, W. Li, Z. Chen, X. Ji, J. Li, Defect-rich and ultrathin N doped carbon nanosheets as advanced trifunctional metal-free electrocatalysts for the ORR, OER and HER, Energy Environ. Sci. 12 (2019) 322–333, https://doi.org/10.1039/C8EE03276A.
[46] M.A. Ahsan, T. He, K. Eid, A.M. Abdullah, M.L. Curry, A. Du, A.R. Puente Santiago, L. Echegoyen, J.C. Noveron, Tuning the intermolecular electron transfer of low-dimensional and metal-free BCN/C_{60} electrocatalysts via interfacial defects for efficient hydrogen and oxygen electrochemistry, J. Am. Chem. Soc. 143 (2021) 1203–1215, https://doi.org/10.1021/jacs.0c12386.
[47] Y. Zheng, Y. Jiao, Y. Zhu, L.H. Li, Y. Han, Y. Chen, A. Du, M. Jaroniec, S.Z. Qiao, Hydrogen evolution by a metal-free electrocatalyst, Nat. Commun. 5 (2014) 3783, https://doi.org/10.1038/ncomms4783.
[48] Y. Wang, G. Sun, L. Chen, Z. Du, X. Li, C. Ye, J. Liu, B. Su, Engineering dual defective graphenes to synergistically improve electrocatalytic hydrogen evolution,

Appl. Surf. Sci. 566 (2021) 150712, https://doi.org/10.1016/j.apsusc.2021.150712.
[49] Y. Liu, N. Ye, X. Li, X. Li, H. Liu, E. Wang, C. Liang, X. Peng, Nitrogen-doped carbon quantum dots via a facile reflux assisted polymerization of N-Methyl-Pyrrolidone for hydrogen evolution reaction, J. Solid State Chem. 293 (2021) 121781, https://doi.org/10.1016/j.jssc.2020.121781.
[50] J.K. Nørskov, J. Rossmeisl, A. Logadottir, L. Lindqvist, J.R. Kitchin, T. Bligaard, H. Jónsson, Origin of the overpotential for oxygen reduction at a fuel-cell cathode, J. Phys. Chem. B 108 (2004) 17886–17892, https://doi.org/10.1021/jp047349j.
[51] Y. Jiao, Y. Zheng, K. Davey, S.-Z. Qiao, Activity origin and catalyst design principles for electrocatalytic hydrogen evolution on heteroatom-doped graphene, Nat. Energy 1 (2016) 16130, https://doi.org/10.1038/nenergy.2016.130.
[52] R. Kronberg, H. Lappalainen, K. Laasonen, Revisiting the Volmer–Heyrovský mechanism of hydrogen evolution on a nitrogen doped carbon nanotube: constrained molecular dynamics *versus* the nudged elastic band method, Phys. Chem. Chem. Phys. 22 (2020) 10536–10549, https://doi.org/10.1039/C9CP06474E.
[53] S. Bawari, N.M. Kaley, S. Pal, T.V. Vineesh, S. Ghosh, J. Mondal, T.N. Narayanan, On the hydrogen evolution reaction activity of graphene–hBN van der Waals heterostructures, Phys. Chem. Chem. Phys. 20 (2018) 15007–15014, https://doi.org/10.1039/C8CP01020J.
[54] L. Hornekær, Ž. Šljivančanin, W. Xu, R. Otero, E. Rauls, I. Stensgaard, E. Lægsgaard, B. Hammer, F. Besenbacher, Metastable structures and recombination pathways for atomic hydrogen on the graphite (0001) surface, Phys. Rev. Lett. 96 (2006) 156104, https://doi.org/10.1103/PhysRevLett.96.156104.